



Molecular dynamics simulations of the deformation behavior of gadolinia-doped ceria solid electrolytes under tensile loading

Yi Sun*, Chen Wang, Yunjun Chen

Department of Astronautics and Mechanics, Harbin Institute of Technology, Harbin 150001, China

HIGHLIGHTS

- The deformation behavior of gadolinia-doped ceria under tensile loading was investigated.
- A martensitic transformation from a fluorite to a rutile or its twin structure was observed.
- A stress-induced pre-transformation occurs before martensitic nucleation.
- The oxygen vacancies can hinder the pre-transformation by disrupting the mechanism.
- The tensile strength shows a fluctuation trend, which accords with the experiments.

ARTICLE INFO

Article history:

Received 28 September 2012

Received in revised form

18 January 2013

Accepted 21 January 2013

Available online 28 January 2013

Keywords:

Molecular dynamics simulation

Gadolinia-doped ceria

Deformation behavior

Stress-induced martensitic transformation

ABSTRACT

Gadolinia-doped ceria (GDC) is a promising candidate electrolyte material for use in intermediate-temperature solid oxide fuel cells (IT-SOFCs). By doping gadolinia during the synthesis process, some oxygen vacancies are generated to promote ionic conductivity. However, the mechanical properties of GDC are severely attenuated by introduced point defects. In the current work, molecular dynamics (MD) simulations are carried out on the uniaxial tensile deformation process of GDC. The GDC is observed to undergo a stress-induced martensitic phase transformation from a fluorite structure to a rutile structure or its twin structure. It is found that the addition of point defects has a significant influence on the phase-transformation behavior of GDC, which limits the further deformation and the loading capacity of the material. The dopant-dependent tensile strength is also obtained and is observed to be consistent with reported experimental measurements.

© 2013 Elsevier B.V. All rights reserved.

1. Introduction

Intermediate-temperature solid oxide fuel cells (IT-SOFCs) have attracted extensive attention because of their high power efficiencies and low operating temperatures. However, the widespread commercialization of SOFCs is impeded by some undeveloped technologies, especially the development of a solid electrolyte material with a sufficient mechanical strength and a high ionic conductivity at working temperatures [1–4]. Ceria-based solid electrolytes are considered the most promising candidate electrolyte materials for IT-SOFCs [5,6]. Kim has analyzed the dependence that the ionic conductivity of the ceria-based solid electrolyte has on the doping cation radius and concluded that the maximum ionic conductivity was obtained by doping Sm^{3+} or Gd^{3+} because the radii of these ions are similar to the radius of Ce^{4+} [7]. Therefore,

gadolinia-doped ceria (GDC) materials have been extensively researched.

Pure ceria has a poor ionic conductivity. The doping of ceria with gadolinia forms a substitutional solid solution. An oxygen vacancy is formed for every two Ce^{4+} ions that are substituted with Gd^{3+} to maintain electroneutrality. Although the oxygen vacancies improve the ionic conductivity significantly, these point defects may also have a serious impact on the mechanical properties of the material. Sato et al. [8] and Ishida et al. [9] have studied the influence of the doping concentration on the fracture stress of GDC by the small punch (SP) and the modified small punch (MSP) methods. Morales et al. investigated Young's modulus and the fracture toughness of GDC by nanoindentation and showed that the gadolinia content had negative effects on the mechanical properties of the material [10].

Molecular dynamics (MD) simulations have been widely used to reveal the micro-mechanism of the deformation behavior of the material. Inaba et al. explained the diffusion behavior of GDC using the MD simulation method [11]. Hayashi et al. applied MD simulations to ceria-based solid solutions with different dopants to

* Corresponding author. Tel.: +86 451 86418124.

E-mail address: sunyi@hit.edu.cn (Y. Sun).

understand the effect of dopants with different radii [12]. Sayle and Sayle adopted MD simulations to investigate CeO₂ nanorods under uniaxial tensile loading and showed that the CeO₂ nanorod underwent a fluorite-to-rutile phase transformation at up to 6% strain [13].

In this work, molecular dynamics simulations were conducted on the uniaxial tensile behavior of GDCs with different doping concentrations. The GDCs were observed to undergo a stress-induced martensitic phase transformation from a fluorite structure to a rutile structure or its twin structure. The influence of oxygen vacancies on the martensitic transformation and the loading capacity was analyzed.

2. Computational model

2.1. Potential

Interionic potential is the key to molecular dynamics simulations. In this work, a semi-ab initio interionic potential by Zhiwei Cui et al. [14,15] was adopted and is expressed as follows:

$$\begin{aligned}\Phi_{++}(r) &= \frac{q_+^2}{4\pi\epsilon_0 r} \\ \Phi_{--}(r) &= a_{--} \left\{ \exp \left[b_{--} \left(1 - \frac{r}{c_{--}} \right) \right] - 2 \exp \left[\frac{b_{--}}{2} \left(1 - \frac{r}{c_{--}} \right) \right] \right\} \\ &\quad + \frac{q_-^2}{4\pi\epsilon_0 r} \\ \Phi_{+-}(r) &= a_{+-} \exp \left[b_{+-} \left(1 - \frac{r}{c_{+-}} \right) \right] + \frac{q_+ q_-}{4\pi\epsilon_0 r}\end{aligned}$$

where q_+ and q_- are the charges of cations and anions, respectively. r is the separation between two ions. ϵ_0 is the vacuum permittivity. a , b , c are potential parameters and tabulated in Table 1.

The Chen–Mobius lattice inversion method [16,17] was employed to characterize the interactions between hetero-species ions, and the quantum-chemical method [18,19] was used to obtain the potential between the ions of the same species by calculating the energies of two identical ions in the gas phase. The Coulomb interaction was calculated using the Wolf algorithm [20]. The potential was verified for a broad class of ionic solids by molecular dynamics simulations, and the ab initio analysis can also be used for the evaluation of other potentials [21,22].

2.2. Model

CeO₂ has a cubic fluorite crystal structure, in which the Ce⁴⁺ ions sit on the face-centered cubic sublattice sites and the O²⁻ ions occupy the tetrahedral interstitial positions. The cell structure of CeO₂ is depicted in Fig. 1. The GDC model was obtained by replacing a number of Ce⁴⁺ ions with Gd³⁺ ions and removing half that number of O²⁻ ions randomly. The schematic diagram of defects in GDC is depicted in Fig. 2, and xGDC refers to the doped materials (CeO₂)_{1-x/100}(GdO_{1.5})_{x/100}. Periodic boundary conditions were applied along all directions. The dimensions of the models were 7.588 nm × 15.176 nm × 7.588 nm before the initial relaxation. The

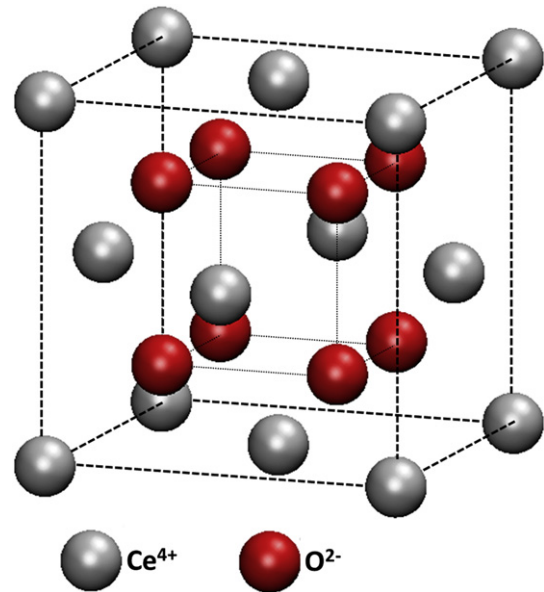


Fig. 1. The cell structure of CeO₂.

model dimension along the tensile direction was enlarged for a better simulation of the fracture process. The simulation system included 65856 atoms for ceria, and the number of atoms was slightly less for GDC because of the removal of oxygen. The models were sufficiently relaxed before the tensile load was applied. The computational model of GDC is depicted in Fig. 3.

All the simulations were conducted using the LAMMPS code [23]. The equations of motion were integrated using the velocity Verlet algorithm with time steps of 2 fs. The NPT ensemble was adopted and implemented with the Nose–Hoover thermostat and the Parinello–Rahaman pressostat. The stresses were calculated using the Virial theorem [24]. The tensile loading was conducted

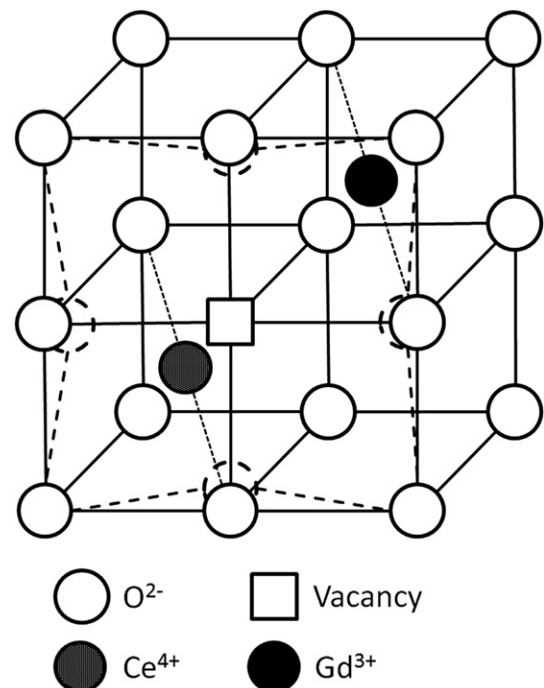


Fig. 2. A schematic diagram of defects in GDC.

Table 1
The parameters of short-ranged potentials of GDC.

	$a(\text{eV})$	b	$c(\text{nm})$
$\text{O}^{2-}-\text{O}^{2-}$	0.77109	7.85216	0.199458
$\text{Ce}^{4+}-\text{O}^{2-}$	0.20	8.46211	0.342512
$\text{Gd}^{3+}-\text{O}^{2-}$	0.20	7.95857	0.340062

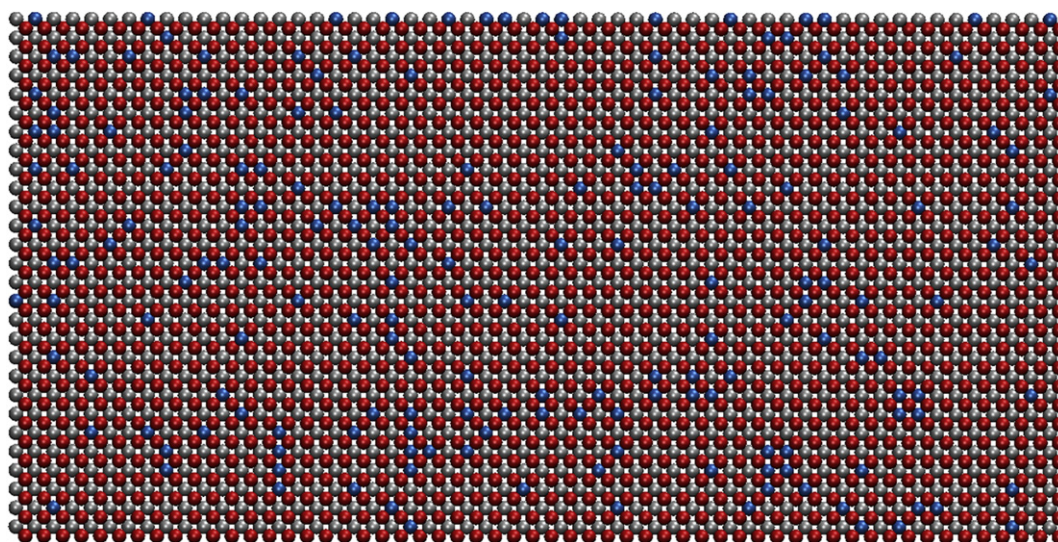


Fig. 3. The computational model of GDC.

over many cycles. Each cycle began with a small abrupt change in the dimension along the $[0\ 1\ 0]$ direction, followed by fixing that dimension and relaxing for 1 ps. The effective strain rate was $5 \times 10^8\ \text{s}^{-1}$.

3. Results and discussion

3.1. The mechanical behavior of GDC under tensile loading

A stress-induced pre-transformation for ceria occurred at a strain of 0.027, causing the whole model to enter the transition phase simultaneously at that point. The two adjacent O^{2-} ions made a relative movement in the tensile direction while remaining unchanged in the other directions, as shown in Fig. 4. Meanwhile, the slope of the stress–strain curve decreased, which indicated a softening of the elastic constant, as shown in Fig. 5. During the transformation, the volumetric strain was continuous and no exothermic peak was found, as shown in Fig. 6 and Fig. 7. Therefore, the pre-transformation is a second-order transformation.

The pre-transformation occurred because of the instability of the sublattice structure. The instability is a result of the decreased frequency of the corresponding mode of the parent phase under tensile loading conditions [25]. Every O^{2-} ion is in a tetrahedral interstitial site, constrained by four cations, and repulsed by neighboring O^{2-} ions, as shown schematically in Fig. 8. When the tensile load was applied in the Y direction, contractions occurred in the X

and the Z directions, thus intensifying the repulsion of the O^{2-} ions. Consequently, the restoring force on O^{2-} was weakened because of the stronger repulsion force acting in the Y direction. The lattice instability and transformation from the fluorite phase to the transition phase occurred when the stress exceeded the threshold.

At a strain of 0.06, a nucleation was observed. The cell structure is depicted in Fig. 9, showing a new phase comprising only the rutile twin structure. In the rutile twin structure, the anions form a distorted HCP structure and the cations form a BCT twin structure. When the tensile load is applied in the $[0\ 1\ 1]$ direction, the rutile structure and the twin structure can both be found after nucleation occurs. The atom configuration is shown in Fig. 10. The rutile structure comprises the distorted HCP derived from the SC and the BCT derived from the FCC as the Bain relation. The cell structures are depicted in Fig. 11.

T. Sayle and D.C. Sayle were the first to propose the possible phase transformation of CeO_2 from the fluorite structure to the rutile structure upon tensile deformation [13]. However, the model that they used was a one-dimensional nanorod, and no rutile twins were found. In the present work, a three-dimensional cubic block is

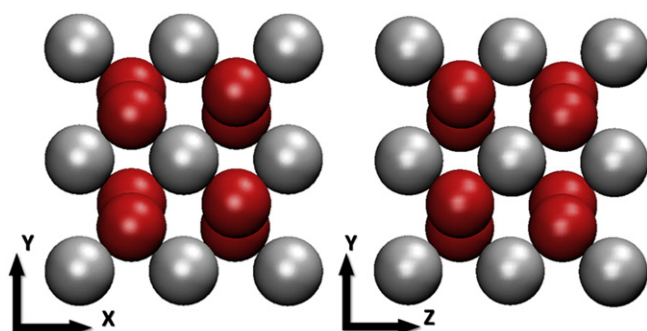


Fig. 4. The cell structure of transition phase of CeO_2 after pre-transformation.

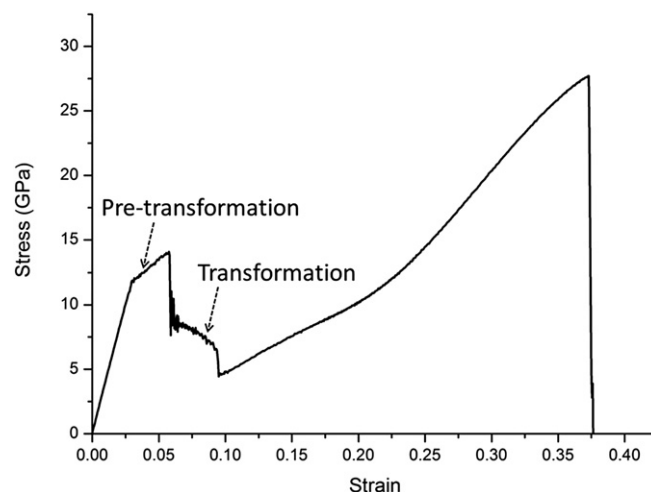


Fig. 5. The stress–strain curve in the $[0\ 1\ 0]$ direction.

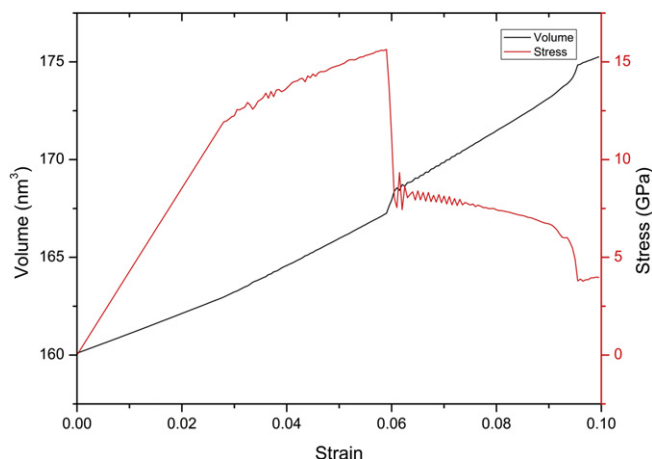


Fig. 6. The volume variation in the transformation.

analyzed with periodic boundary conditions. As the phase transformation will result in significant changes to the lattice structure, the appearance of rutile twins may be to accommodate the shear strain caused by the boundary constraints.

When nucleation occurs, the stress decreases abruptly because of the softening of the new phase, and most of the pre-transformation phase reverts into the fluorite phase as the new rutile twins accommodate most of the strain. Some of the transition phase can be still found at the phase interface. There is an exothermic peak as well as abrupt changes to the stress and to the volume during the transformation, as shown in Figs. 6 and 7. Therefore, the phase transformation is a first-order transformation.

The symmetry of the structure changes during the transformation. The centro-symmetry parameters of cations were computed to show the transformation process shown in Fig. 12 via the following formula from Kelchner et al. [26].

$$P = \sum_{i=1}^4 |\mathbf{R}_i + \mathbf{R}_{i+4}|^2$$

The centro-symmetry parameter for the cations in the fluorite structure is 0 and is green in color. The cation parameter in the rutile twin structure is approximately 5.75 and is blue in color. The cation parameter in the transition phase is approximately 0.9 and is white in color.

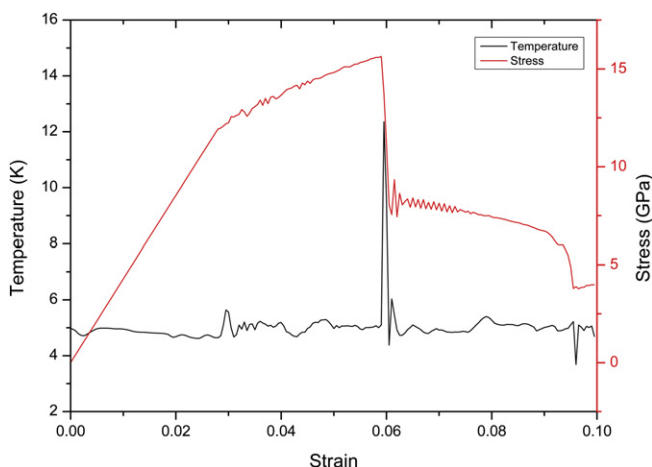


Fig. 7. The temperature variation in the transformation.

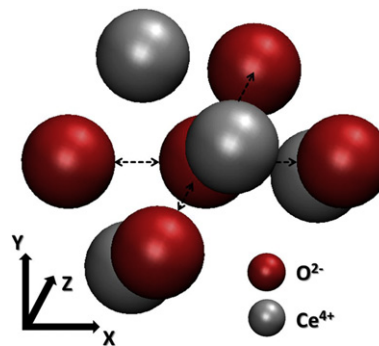


Fig. 8. The schematic diagram of stress-induced pre-transformations.

The rutile twin phase propagates as the strain increases until the phase transformation is complete. The phase transformation accelerates during the process, and an avalanche transformation occurs toward the end, as shown in Fig. 5. This result occurs because the rutile twin phase expands in the X direction and contracts in the Z direction relative to the fluorite phase, thus producing interacting stresses between the two phases because of the boundary constraints. When the rutile twin phase is large enough, the interacting stresses may significantly facilitate the transformation process.

A reverse transformation can be observed when the model is unloaded after the stress-induced phase transformation from the fluorite structure to the rutile twin structure. The deformation recovers completely, and the stress along the [0 1 0] direction vanishes as the tensile strain is reduced to zero. The pseudo-elasticity behavior and the hysteresis can be observed in the stress–strain curve shown in Fig. 13. Therefore, the phase transformation should be a stress-induced martensitic transformation.

For the GDC samples with a doping concentration of less than 12GDC, the whole model undergoes a stress-induced martensitic transformation before the fracture occurs. After the transformation, the rutile twin phase is still capable of bearing the tensile load until the tensile strength is reached and instability occurs. Two amorphous surfaces form at the crack, and the rest of the model reverts back into the fluorite phase through reverse transformation, as shown in Fig. 14.

For the GDC samples with a doping concentration of approximately 16GDC, only a part of the model can be transformed into the rutile phase because of the hindrance caused by the introduced oxygen vacancies. The transformation ends at the region where the oxygen vacancies are concentrated. The instabilities and

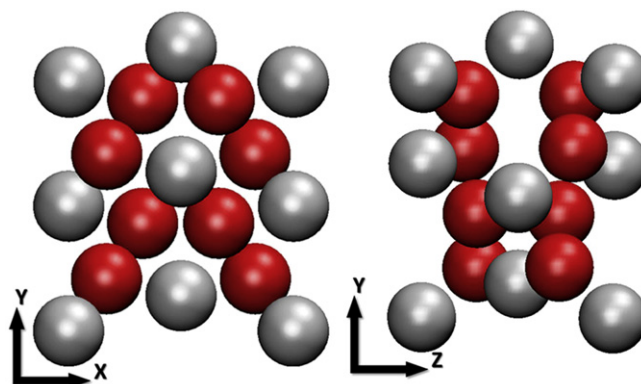


Fig. 9. The cell structure of rutile twin phase of CeO₂ after transformation.

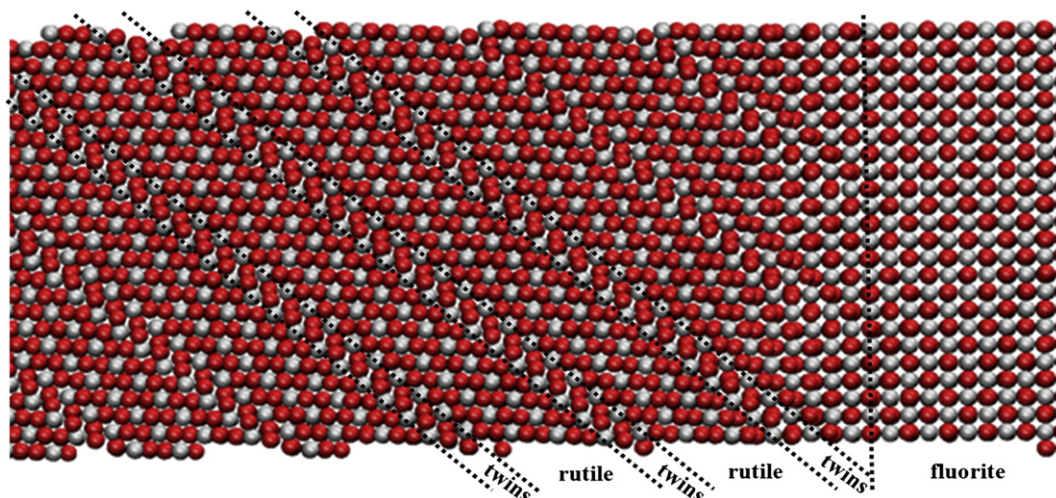


Fig. 10. The coexistence of the rutile structure and the twin structure after the nucleation under tensile loading in the $[0\ 1\ 1]$ direction.

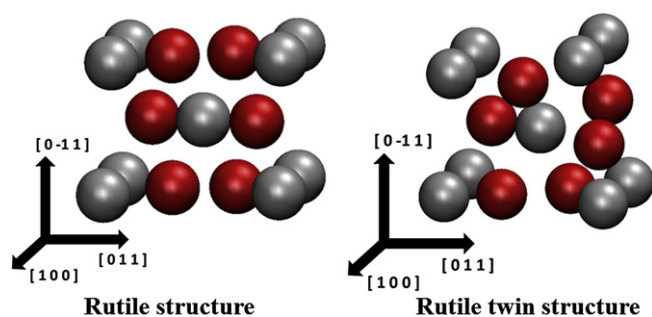


Fig. 11. The cell structure after transformation under tensile loading in the $[0\ 1\ 1]$ direction.

the fractures occur at the phase interface when the stress that is exerted equals the interfacial tensile strength. This stress peak is lower than the stress peak before the transformation; hence, it can be inferred that the phase interface causes the structure to become more unstable because of the interaction between the two phases.

For the GDC samples with a doping concentration of more than 20GDC, the fracture occurs directly at the weakest region without any obvious nucleation or propagation. However, some regional transformation can still be found in the instability zone, as shown in Fig. 15, where only a part of the model is shown.

3.2. Effects of defects on mechanical properties

When the CeO_2 is doped with Gd_2O_3 , Gd^{3+} ions occupy the locations that were previously occupied by Ce^{4+} ions, and one O^{2-} ion for every two substituted cations is removed to maintain electro-neutrality. As a consequence, two types of point defects are introduced, as shown in Fig. 2. Although both defects cause the lattice structure to be different, the main influence on the lattice structure comes from the oxygen vacancies because the radius of Gd^{3+} is similar to that of Ce^{4+} .

3.2.1. Effects of defects on Young's modulus

Young's moduli of the GDCs were obtained by fitting the linear part of the stress–strain curves. Young's modulus of the GDC decreases with an increasing defect concentration, as shown in Fig. 16.

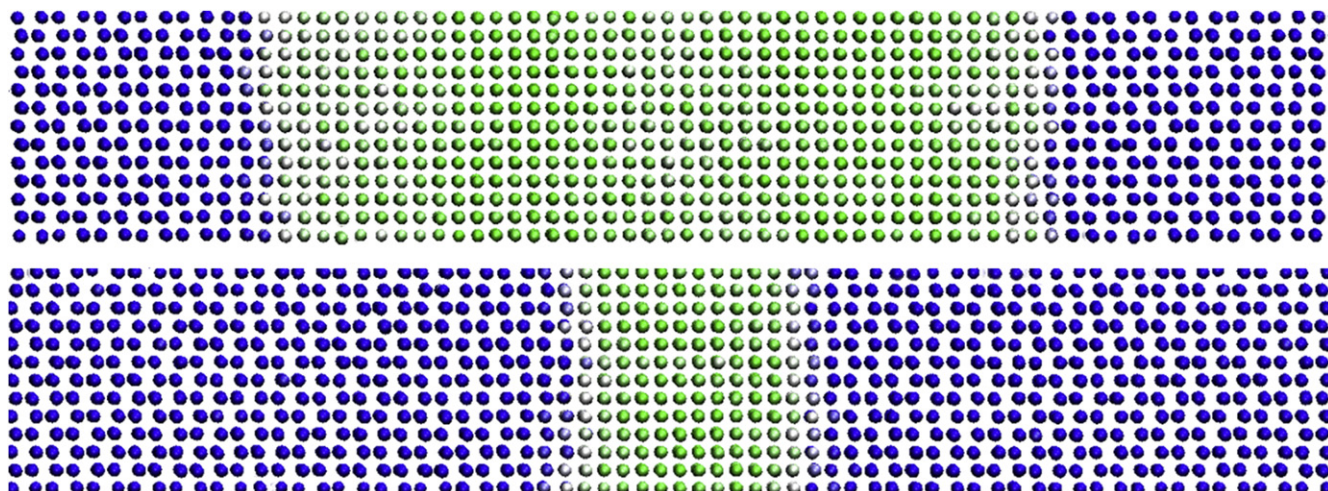


Fig. 12. The nucleation and the propagation of the rutile twin phase.

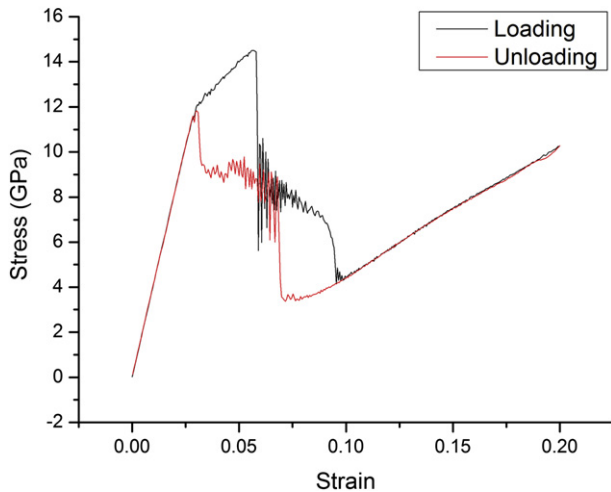


Fig. 13. The pseudo-elasticity behavior and the hysteresis of CeO_2 .

3.2.2. The effects of defects on stress-induced martensitic transformation

Fig. 17 shows the effects of the defects on the phase transformation behavior of the GDC. It can be observed from the atomic configurations that the pre-transformation of the whole model disappears gradually as the doping concentration increases. Correspondingly, the elastic constant softening that is caused by the pre-transformation also disappears gradually, which can be observed from the stress–strain curves. Therefore, pre-transformation can be hindered by the presence of oxygen vacancies. As mentioned above, the mechanism of the pre-transformation is a vibrational instability caused by the intense repulsion between the O^{2-} ions. The absence of some O^{2-} ions weakens the repulsion and disrupts the mechanism.

The martensitic transformation can be facilitated by pre-transformation because the transition phase is more similar to martensite than is the parent phase. As pre-transformation can be hindered by the oxygen vacancies, the martensitic nucleation will be hindered and the critical stress will increase as the defect concentration increases, as shown in Fig. 18.

During the propagation of the rutile twin phase, hindrance can also be observed in the stress–strain curve, as shown in Fig. 17. In pure CeO_2 , the rutile twin phase grows smoothly as the strain increases. However, the process is hindered several times in GDCs, which is also indicated by the rough part of the stress–strain curves exhibited by the GDCs. When the propagation of the rutile twin

phase is blocked at the region where the oxygen vacancies are concentrated at, the stress increases because no more strain can be accommodated by the transformation. For GDCs with low defect concentrations, the transformation can be restarted as the stress is increased to a level that is high enough to overcome the hindrance. For GDCs with high defect concentrations, the stress equals the tensile strength, causing fractures to occur at the phase interface.

3.2.3. The effects of defects on the tensile strength of GDC

Fig. 19 shows the variation of the tensile strength of the GDC samples with the doping concentration. It can be observed that the fluctuation tendency may be divided into three periods:

- (1) GDC models that had low doping concentration underwent a complete martensitic transformation from the fluorite phase to the rutile twin phase before fracturing. In addition, the loading capacity of the rutile twin phase was greater than the critical nucleation stress of the fluorite phase. Therefore, the loading capacity of the rutile twin phase determines the tensile strength of the GDCs, which decreases dramatically as the doping concentration increases within this range.
- (2) In GDCs that were doped at higher concentrations, the tensile strengths are determined by the critical nucleation stresses. As shown in Fig. 18, the oxygen vacancies hinder the transformation and increase the critical nucleation stress, thus increasing the tensile strength within this range.
- (3) When the doping concentration is high enough, the tensile strengths are determined by the loading capacities of the fluorite phase because no transformation nucleation occurs before fracturing. The oxygen vacancies distort the lattice and cause the structure to be attenuated. Therefore, the tensile strength decreases as the doping concentration increases.

The fluctuation trend is in accordance with the trend of experimental fracture strengths, which have been reported by Ishida et al. [9] and are shown in Fig. 20. These authors estimated the fracture properties of rare earth-doped ceria ceramics using the modified small punch method. The fracture strength was calculated from the fracture load by using the following equation that is ascribed to the finite element method.

$$\sigma_{\text{SP}} = \frac{P}{t^2} (1 + \nu) \left[0.485 \ln \frac{a}{t} + 0.52 + \frac{3}{2\pi(1 + \nu)} \right]$$

The abnormal increase of the fracture strength as the doping concentration increased was also reported by Sato et al. [8].

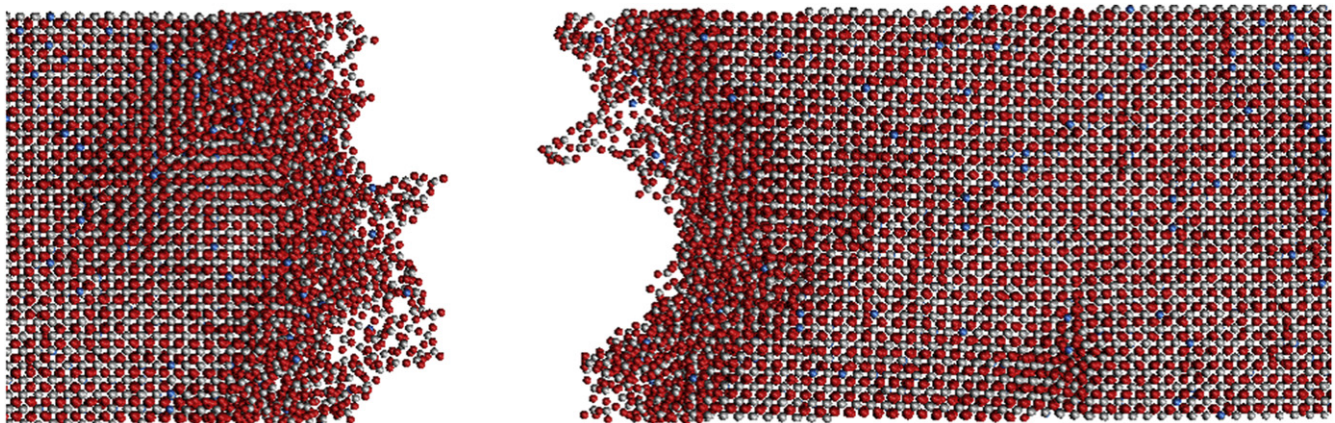


Fig. 14. The fracture of the model specimen.

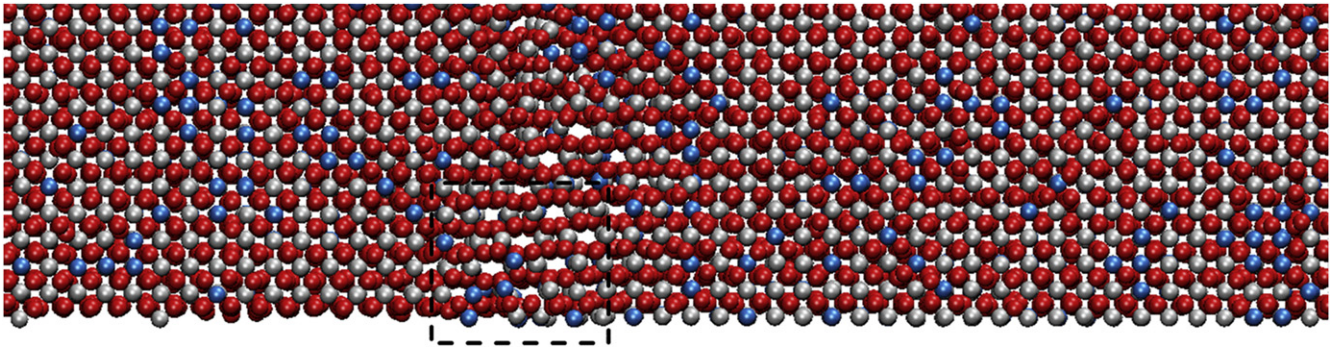


Fig. 15. The regional transformation in the instability zone.

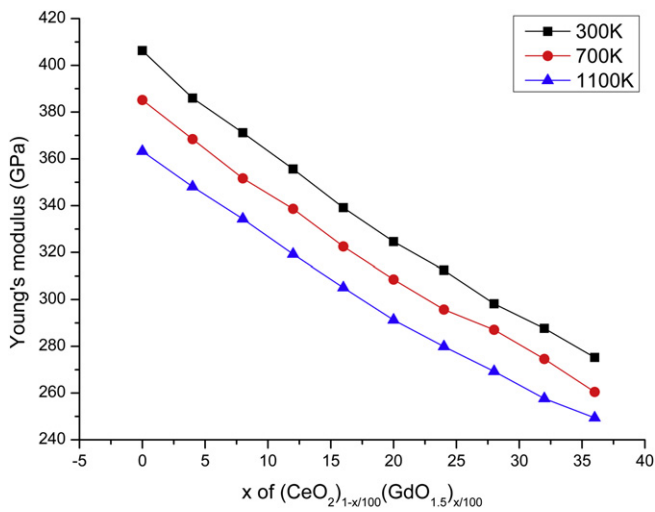


Fig. 16. The effects of the defects on Young's modulus.

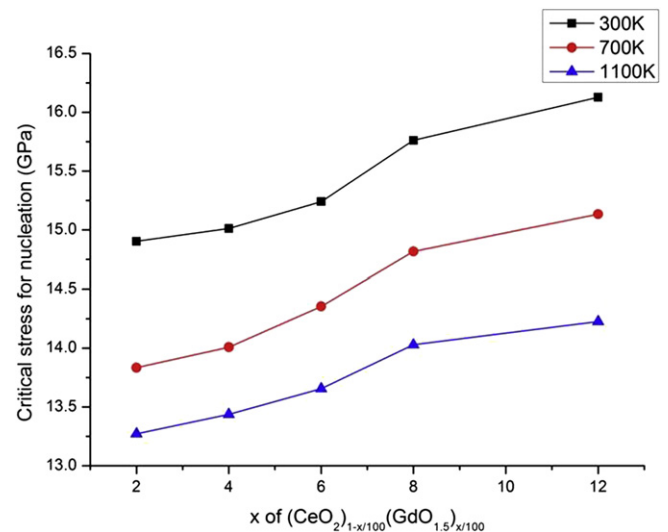


Fig. 18. The effects of the defects on the critical nucleation stress.

The tensile strengths obtained in this work are quantitatively much larger than the experimental values. Such a discrepancy may be because the present model is a nanoscale single crystal block and not a macroscopic polycrystalline specimen. The absolute value of the tensile strength may be significantly influenced by the size effects and the vacancies that are concentrated on the polycrystalline

grain boundaries. However, Fig. 20 shows some qualitative agreement on the abnormal fluctuations of the tensile strength. Therefore, this work is of practical importance and is a promising beginning for further studies.

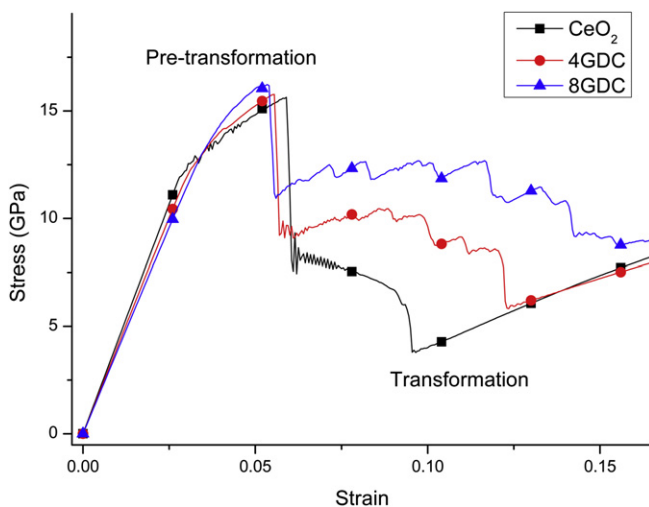


Fig. 17. The effects of the defects on the transformation.

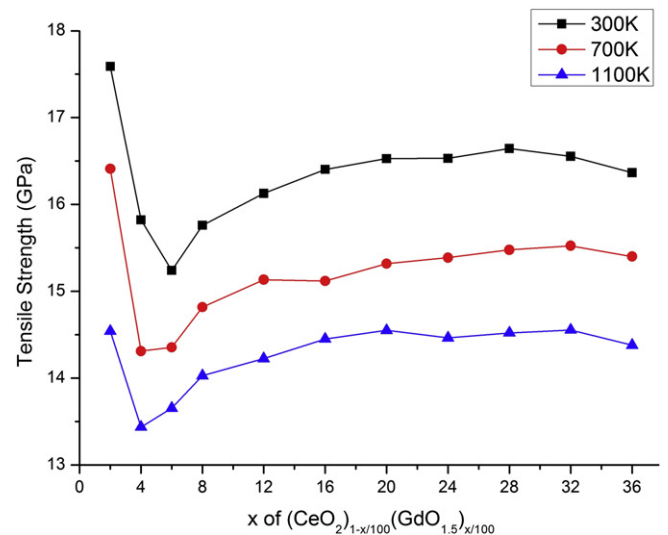


Fig. 19. The effects of the defects on the tensile strength of GDC.

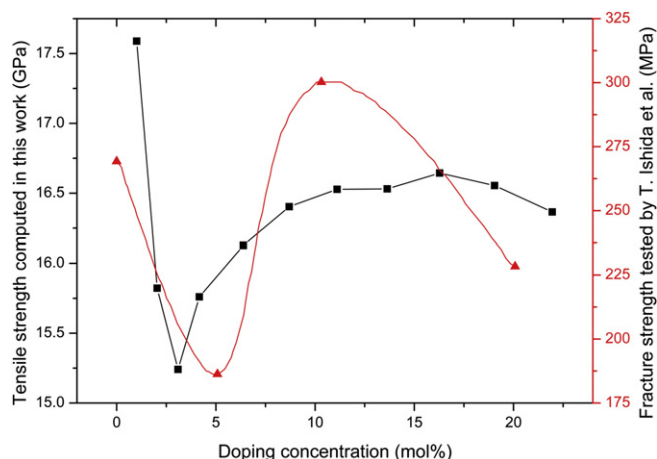


Fig. 20. A comparison of the evaluated tensile strength with experimental values.

4. Conclusions

In the present work, the mechanical behavior of GDC under uniaxial tensile loading and the effects of doping concentration and temperature on the mechanical properties were investigated using MD simulations. The main results can be summarized as follows:

- A stress-induced pre-transformation that is caused by vibrational instability occurs before martensitic nucleation.
- Under uniaxial tensile loading in the $[0\ 1\ 0]$ direction, CeO_2 and GDCs with low doping concentrations undergo a reversible stress-induced martensitic transformation from a fluorite structure to a rutile twin structure. When the load is applied in the $[0\ 1\ 1]$ direction, the rutile structure and the rutile twin structure coexist after the transformation.
- When the doping concentration is low, the tensile strength is determined by the loading capacity of the rutile twin phase, which is reduced by the defects. When the doping concentration is increased, the tensile strength is determined by the critical nucleation stress of transformation, which is enlarged by the

oxygen vacancies that hinder the martensitic transformation. When the doping concentration is high enough, the tensile strength is determined by the loading capacity of the fluorite phase, which decreases with an increasing number of defects.

Acknowledgments

The present work was supported by the National Natural Science Foundation of China (10972066) and the Research Fund for the Doctoral Program of Higher Education of China (20122302110020).

References

- [1] K.R. Reddy, K. Karan, J. Electroceram. 15 (2005) 45–56.
- [2] J.W. Fergus, J. Power Sources 162 (2006) 30–40.
- [3] J.P.P. Huijsmans, F.P.F. van Berkel, G.M. Christie, J. Power Sources 71 (1998) 107–110.
- [4] O. Bellon, N.M. Sammes, J. Staniforth, J. Power Sources 75 (1998) 116–121.
- [5] H. Inaba, H. Tagawa, Solid State Ionics 83 (1996) 1–16.
- [6] S.W. Zha, C.R. Xia, G.Y. Meng, J. Power Sources 115 (2003) 44–48.
- [7] D.J. Kim, J. Am. Ceram. Soc. 72 (1989) 1415–1421.
- [8] K. Sato, H. Yugami, T. Hashida, J. Mater. Sci. 39 (2004) 5765–5770.
- [9] T. Ishida, F. Iguchi, K. Sato, T. Hashida, H. Yugami, Solid State Ionics 176 (2005) 2417–2421.
- [10] M. Morales, J.J. Roa, X.G. Capdevila, M. Segarra, S. Pinol, Acta Mater. 58 (2010) 2504–2509.
- [11] H. Inaba, R. Sagawa, H. Hayashi, K. Kawamura, Solid State Ionics 122 (1999) 95–103.
- [12] H. Hayashi, R. Sagawa, H. Inaba, K. Kawamura, Solid State Ionics 131 (2000) 281–290.
- [13] T.X.T. Sayle, D.C. Sayle, ACS Nano 4 (2010) 879–886.
- [14] Z.W. Cui, Y. Sun, Y.J. Chen, J.M. Qu, Solid State Ionics 187 (2011) 8–18.
- [15] Z.W. Cui, Y. Sun, J.M. Qu, Solid State Ionics 226 (2012) 24–29.
- [16] S. Zhang, N.X. Chen, Phys. Rev. B 66 (2002) 64106.
- [17] S. Zhang, N.X. Chen, J. Chem. Phys. 118 (2003) 3974–3982.
- [18] H. Ohta, S. Hamaguchi, J. Chem. Phys. 115 (2001) 6679–6690.
- [19] H. Ohta, A. Iwakawa, K. Eriguchi, K. Ono, J. Appl. Phys. 104 (2008) 73302.
- [20] D. Wolf, P. Keblinski, S.R. Phillpot, J. Eggebrecht, J. Chem. Phys. 110 (1999) 8254–8282.
- [21] Z.W. Cui, F. Gao, Z.H. Cui, J.M. Qu, J. Power Sources 207 (2012) 150–159.
- [22] Z.W. Cui, F. Gao, Z.H. Cui, J.M. Qu, Modell. Simul. Mater. Sci. Eng. 20 (2012) 15014.
- [23] S. Plimpton, J. Comput. Phys. 117 (1995) 1–19.
- [24] M. Zhou, Proc. R. Soc. London Ser. A-math. Phys. Eng. Sci. 459 (2003) 2347–2392.
- [25] G. Kostorz, P. Haasen, Phase Transformations in Materials, WILEY-VCH Verlag GmbH, Weinheim, 2001.
- [26] C.L. Kelchner, S.J. Plimpton, J.C. Hamilton, Phys. Rev. B 58 (1998) 11085–11088.